

Full Waveform Inversion using the Wasserstein metric for ultrasound transducer array based NDT

D Rossato¹, T A R Passarin², G P Pires³ and D R Pipa²

¹ Department of Electronics Engineering, Universidade Tecnológica Federal do Paraná, Curitiba, BR

² CPGEI, Universidade Tecnológica Federal do Paraná, Curitiba, BR

³ Petrobras, BR

E-mail: danielrossato@utfpr.edu.br

Abstract. Ultrasonic imaging methods often assume linear direct models, while in reality, many nonlinear phenomena are present, e.g. multiple reflections. A family of imaging methods called Full Waveform Inversion (FWI), which has been developed in the field of seismic imaging, uses full acoustic wave simulations as direct models, taking into account virtually all nonlinearities, which can ultimately enhance the accuracy of ultrasonic imaging. However, the problem of cycle skipping – the existence of many local minima of the Least Squares (L2) misfit function due to the oscillatory nature of the signals – is worsened when FWI is applied to ultrasound data because of a lack of low-frequency components. In this paper, we explore the use of the squared Wasserstein (W2) Optimal Transport Distance as the metric for the misfit between the acquired and the synthetic data, applying the method to Nondestructive Evaluation with ultrasonic phased arrays. An analytical continuous time-domain derivation of the adjoint acoustic field related to the W2 misfit is presented and used for the computation of the gradients. To cope with the computational burden of FWI, we apply a low-memory strategy that allows for the computation of the gradients without the storage of the full simulated fields. The GPU implementation of the method (in CUDA language) is detailed, and the source code is made available. Six prototypical cases are presented, and the corresponding sound speed maps are reconstructed with FWI using both the L2 and the W2 misfit functionals. In five of the six cases, the pixel-wise sum of squared errors obtained with W2 was at least one order of magnitude lower than that obtained with L2, with an increase in the gradient computation time not exceeding 2%. The results highlight both the adequacy of the W2 misfit for ultrasonic FWI with phased arrays and its computational feasibility.

Keywords: full-waveform inversion, optimal transport, non-destructive testing, ultrasound

Submitted to: *Inverse Problems*

1. Introduction

In Non-Destructive Testing (NDT), ultrasonic imaging is a widely used technique to evaluate the internal structure of specimens. If the data is acquired using transducer arrays [1], it is possible to form an image - a reflectance map - of the interior of the specimen, usually by Delay-and-Sum (DAS) algorithms such as the Synthetic Aperture Focusing Technique (SAFT) and the Total Focusing Method (TFM) [2]. However, DAS imaging algorithms are based on a linear observation model and, thus, do not take into account non-linear phenomena such as multiple reflections, shading, and unknown materials, among other common occurrences in ultrasonic testing. This severely limits the type and amount of information that can be extracted from the test.

In the seismic prospecting literature, one commonly studied imaging method is Full Waveform Inversion (FWI) [3, 4]. This technique uses the whole soundwave data from seismic surveys to estimate a sound velocity map of the region of interest, instead of a reflectance map like with DAS. FWI has the potential to extract more accurate and complete data from the survey, but is a greatly costlier and more complex technique [5]. Recent advances in computational power allow for its use in ever greater domains [6]. Although it is primarily used in seismic imaging, it has also been applied in medical imaging [7].

1.1. Full Waveform Inversion

The conceptual foundation for FWI was laid by Albert Tarantola. In his seminal work [3], he framed seismic inversion within a probabilistic framework, proposing the use of the full seismic waveform rather than relying solely on traveltimes information. Tarantola introduced the concept of minimizing a misfit function between observed and simulated seismic data, incorporating model regularization to stabilize the inversion.

At the same time, Lailly [8] independently explored similar ideas, linking FWI to the adjoint-state method, which dramatically reduces the computational cost of gradient calculations in optimization problems. This period established the theoretical underpinnings of FWI as a nonlinear optimization problem.

Although the theory was well-formulated, practical implementation faced severe challenges. First and foremost, the numerical solution of the wave equation in realistic 2D or 3D settings was computationally prohibitive. Modern hardware mitigated this problem, but other two main obstacles remain: (1) inversion tends to converge to local minima when the initial model is far from the true model, due to the cycle-skipping phenomenon, and (2) the method is highly sensitive to inaccuracies in the data, such as noise and mismatches in the amplitude of the signals.

During this period, FWI was mainly explored for simple, synthetic models, often in 1D or 2D media. A classic paper by Gauthier et al. [9] is often cited as the first practical demonstration of FWI for a 2D acoustic model, showing the feasibility of retrieving detailed subsurface structures from FWI.

Techniques such as multiscale approaches – starting from low frequencies and gradually incorporating higher frequencies – proposed by Bunks et al. helped mitigate cycle-skipping [10]. During this period, Pratt et al. introduced methods such as Frequency-domain FWI and the use of different objective functions, as well as Gauss-Newton methods for the minimization instead of simple gradient descent [11, 12].

The aforementioned advances in computational hardware marked a turning point for FWI, when high-performance computing and parallelization made large-scale 2D and later 3D inversions feasible. While Virieux and Operto [4] provided a widely cited review consolidating the theoretical, numerical, and practical aspects of FWI, several works applying FWI to real-world data were published [13, 14, 15, 16, 17], only to name a few. For a more in-depth discussion of the history of FWI, Huang et al. [5] provide a comprehensive review.

1.2. Applications of FWI in NDT

Even considering that ultrasound NDT and seismic surveys have very different scales, excitation methods, acquisition methods, materials and subjects, both are techniques for extracting information about sub-surface structures from the acoustic speed of their materials using sound wave propagation. Therefore, FWI should be useful for ultrasound NDT as well [18, 19, 20, 21]. However, since FWI has difficulties in media with abrupt sound speed changes [13], which are the norm in NDT, the cycle-skipping problem [22] is amplified. This can be addressed with cycle-skipping resistant misfit metrics, for example, those based on envelope [23] or optimal transport [24]. Another approach is multi-frequency inversion, although its performance is hampered by band-limited signals [25], which is the case of ultrasonic signals.

This paper proposes a method to apply FWI in NDT, detailing and continuing the work laid out in [21], using the simulation framework of [20], which implements Perfectly Matched Layers to avoid spurious reflections at the borders of the simulation domain [26]. We employ the low-memory implementation first suggested in [27] and further developed in [28], detailed in Section 3.2.

The novelty of this paper is twofold. First, we propose a novel source term based on the Wasserstein distance, derived from the continuous analytic solution to the optimal transport problem, in contrast to the source term from the discrete solution proposed in [29]. Second, we devise domain-specific memory use exploits for GPU-based acceleration of the acoustic wave simulation. These exploits are based on the fact that, in acoustic wave simulation, each point calculation depends only on past values of the same point and its spatial neighbors. This is exploited in two ways: first, points in the same time instant can be computed in parallel, which enables the efficient use of GPUs. Second, the points can be grouped in a way that minimizes the number of memory accesses by explicitly controlling the GPU cache memory.

1.3. Paper Structure

The remainder of the paper is organized as follows. In Section 2, we review the Full Waveform Inversion method, the problem known as cycle-skipping, and misfit metrics proposed to mitigate it, as well as the Wasserstein metric. Section 3 presents the proposed method for FWI in NDT, detailing the parallelization using CUDA and memory use optimization specific to the acoustic simulation. The simulated test setups for evaluation are also detailed. Section 4 shows the test results, which are discussed in Section 5 along with conclusions and directions for future work.

2. Background

Full Waveform Inversion is a numerical gradient based technique that tries to match observed and simulated soundwaves by refining the simulated medium estimate until the observed and simulated data are sufficiently similar [3, 9, 4]. It uses the Adjoint State Method to calculate the otherwise exceedingly costly gradient. Figure 1 shows this workflow. The algorithm starts with an observed acoustic field and the excitation waveform, called forward source. Then, with an initial guess for the sound speed model, a simulated field is created using the forward source. The observed and simulated fields are compared to generate a misfit metric and the misfit gradient w.r.t the speed model using the Adjoint State Method. This gradient is used to update the speed model estimate, iterating this cycle until a stop criterion is satisfied.

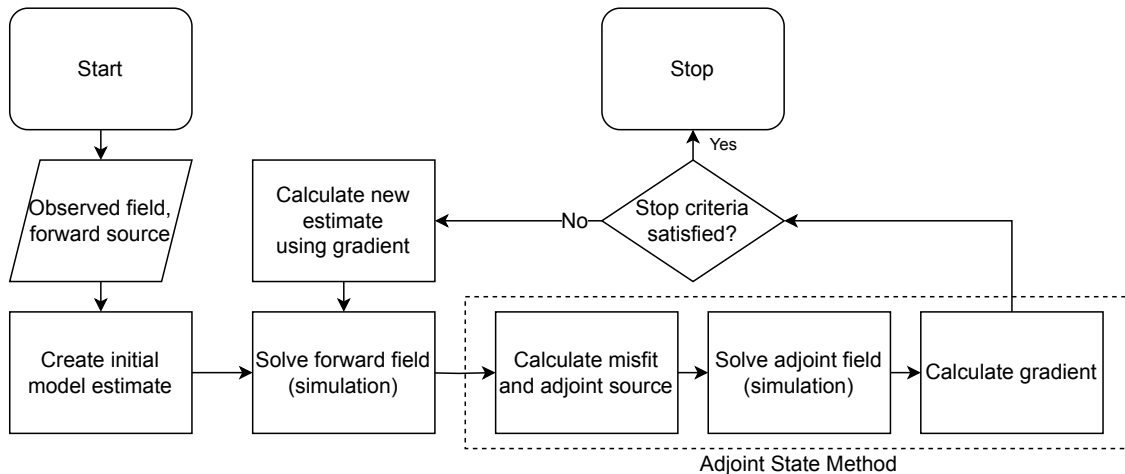


Figure 1: FWI algorithm.

2.1. Forward problem

The wave propagation in a given medium can be modeled by the visco-elastic equation or the acoustic wave equation. Our approach uses the latter, given by [1, 30]

$$\left[\frac{\partial^2}{\partial t^2} - \theta(x)\nabla^2 \right] u(x, t) = f(x, t), \quad (1)$$

where $u(x, t)$ is the acoustic pressure at the position x and time instant t , $\theta(x)$ is the wave propagation speed field (henceforth referred to as “speed field” for brevity) at the position x , and $f(x, t)$ represents the external sources of pressure (usually transducers), referred to as source term. The speed field is time-invariable, and the source term is an attribute of the ultrasonic excitation/acquisition system.

Since the term multiplying $u(x, t)$ contains only constants and linear operators, this equation is linear with respect to $u(x, t)$, and can be written as

$$L(\theta)u(x, t) = f(x, t), \quad L(\theta) = \left[\frac{\partial^2}{\partial t^2} - \theta(x)\nabla^2 \right] \quad (2)$$

where $L(\theta)$ is called the acoustic wave operator for a speed field $\theta(x)$. Dropping the variables for the sake of clarity, we have

$$Lu = f \quad (3)$$

$$L = \left[\frac{\partial^2}{\partial t^2} - \theta(x)\nabla^2 \right]. \quad (4)$$

2.2. Gradient computation using the Adjoint State Method

The FWI algorithm minimizes a misfit metric $J(\theta)$ between the observed and simulated waves. Conventionally, this metric is the L_2^2 distance between the signals [31], given by

$$J(\theta) = \frac{1}{2} \sum_r \int_0^T (u(x_r, t; \theta) - u_0(x_r, t))^2 dt \quad (5)$$

where x_r are the locations in space of the receivers r , u_0 is the observed signal, and $u(\cdot, \cdot; \theta)$ is the simulated acoustic field on the estimated medium θ .

To numerically compute the gradient $\frac{\partial J}{\partial \theta}$, one would have to perturbate each dimension of θ and obtain the resulting variation in $J(\theta)$. However, θ has usually upwards of tens of thousands of parameters, and each calculation of J needs a costly simulation. The solution is to use the Adjoint State Method [31], which allows us to compute the gradient with only one additional simulation. This method exploits the fact that, for the acoustic wave equation (which is self-adjoint),

$$\frac{\partial J(\theta)}{\partial \theta} = - \int_I \tilde{u} \frac{\partial L}{\partial \theta} u dt \quad (6)$$

$$\text{subject to } Lu = s \quad (7)$$

$$L\tilde{u} = \frac{\partial J}{\partial u} = \tilde{s}, \quad (8)$$

where \tilde{u} is the adjoint field, calculated by a new acoustic simulation in the same speed field, but using the adjoint source term \tilde{s} instead of the source term s . This adjoint source \tilde{s} is given by the derivative of the misfit metric J w.r.t to u . For the L_2^2 metric, this source term is given by

$$\tilde{s}(x, t) = \begin{cases} u(x, t; \theta) - u_0(x, t), & \text{for } x = x_r \\ 0, & \text{elsewhere} \end{cases}. \quad (9)$$

Furthermore, since

$$\frac{\partial L}{\partial \theta} = \frac{\partial \left[\frac{\partial^2}{\partial t^2} - \theta(x) \nabla^2 \right]}{\partial \theta} = -\nabla^2, \quad (10)$$

we can turn (6) into

$$\frac{\partial J(\theta)}{\partial \theta} = \int_I \tilde{u} \nabla^2 u \, dt, \quad (11)$$

i.e., the gradient can be obtained by integrating the multiplication between the Laplacian of the acoustic field by the adjoint field, which is obtained by doing a single additional simulation, using the adjoint source \tilde{s} (9) instead of s .

2.3. Misfit metrics and Cycle-skipping

FWI is known to suffer from the cycle-skipping phenomenon. This occurs in the commonly used L_2^2 misfit metric because similar oscillatory signals, when time-shifted with respect to each other, produce an oscillating misfit (with local minima) [22], as shown in Figure 2. Different misfit metrics have been proposed to tackle this problem, such as the envelope of the signal [23, 32, 33], matched filters in the frequency domain [34], and optimal transport [24].

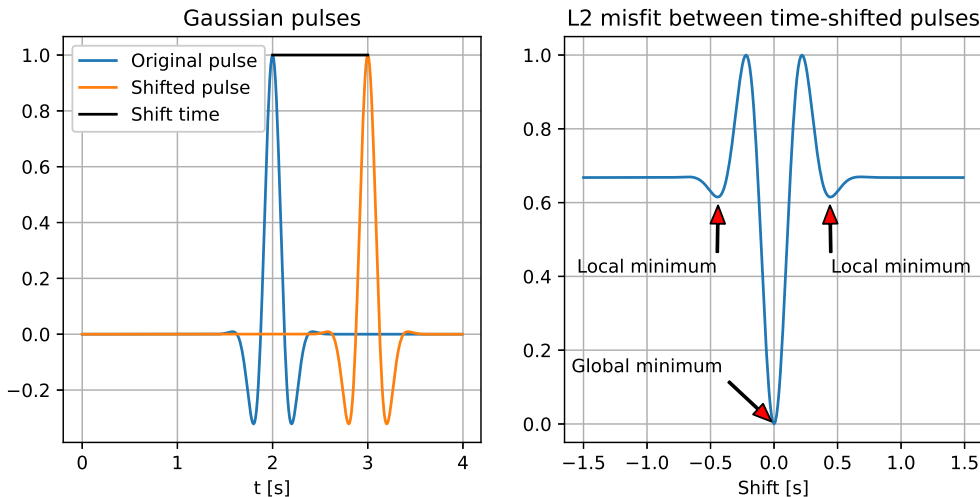


Figure 2: Cycle-skipping phenomena in L_2^2 misfit for time-shifted oscillatory signals.

2.4. Wasserstein distance as misfit metric for FWI

Optimal transport deals with the transformation of one Probability Density Function (PDF) into another with minimum transport work [35]. The Wasserstein distance is one metric of the work necessary to make such a transformation, and can also be interpreted as a measure of the similarity between PDFs [24, 29]. This distance has been successfully applied in seismic FWI as a misfit metric in place of the L_2^2 distance.

Since PDFs have some restrictions – namely, positivity and unitary mass balance – and seismic signals do not conform to them, a transformation is necessary prior to computing the misfit. Many approaches have been proposed, such as separation of the negative and positive portions of the signals, linear offset and scaling [15], and time offsets [17]. One alternative is to use the dual of the Wasserstein optimization program [16].

3. Methodology

3.1. Low memory parallelized acoustic simulation

Since FWI relies on several acoustic simulations and these are computationally costly, it is vital to accelerate this bottleneck. This paper adapts the framework presented in [21], further detailed here. To numerically solve the acoustic wave equation (1), it must be discretized in both time and space. First we discretize in time and isolate the $u(x, t + 1)$ term, obtaining

$$u(x, t + 1) = c^2(x)\nabla^2 u(x, t) + 2u(x, t) - u(x, t - 1) + f(x, t) \quad (12)$$

which is the update formula, i.e., the equation that determines how each pressure point is updated each time iteration. This equation has an important property that can be exploited to improve performance: each time instant depends only on the last two time instants. This can be exploited in two ways: first, it implies the possibility of parallelization, since for every space point x at the instant $t + 1$, its pressure is independent of the other points in $t + 1$, depending only on t and $t - 1$. Second, since only the pressure values from the last two time instants are needed, one does not need to store all the pressure values. Storing only these two time instants makes the implementation low memory, enabling longer simulations and allowing for more efficient use of RAM.

The CUDA [36] framework is used to parallelize the algorithm. In our parallelization schema, each point $u(x)$ is calculated by a different thread. Although this approach alone improves performance, several steps can be made to further optimize the algorithm.

Modern CUDA hardware can execute thousands of threads simultaneously, but only if these are grouped into blocks, typically containing 32×32 threads. Therefore, to fully utilize hardware capabilities, our algorithm divides the simulation domain into subdomains comprising 32×32 points. Each subdomain is then calculated by a thread block, as shown in Figure 3.

Each thread updates the pressure value of its respective space position, according to Equation (12). Despite its apparent simplicity, its computational cost can be relatively high depending on the precision of the Laplacian operator ∇^2 approximation. In the continuous form,

$$\nabla^2 f = \sum_{i=1}^n \frac{\partial^2 f}{\partial x_i^2} \quad (13)$$

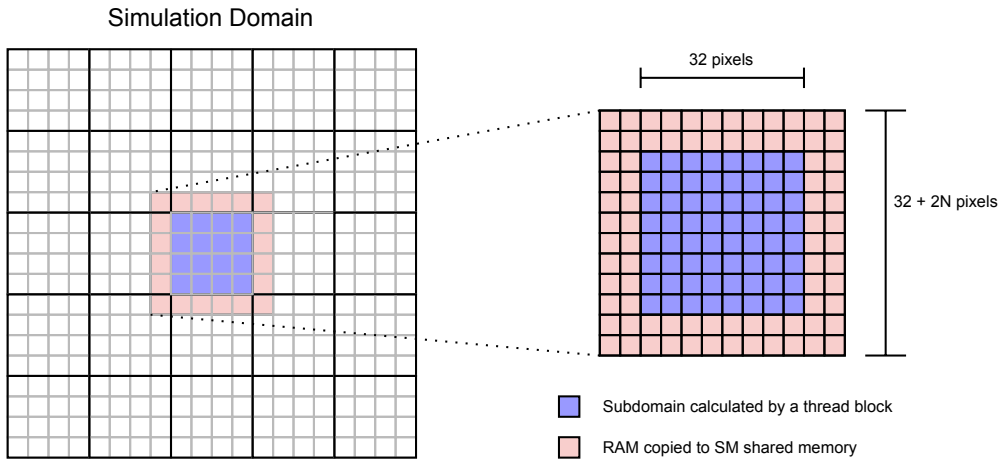


Figure 3: Division of the simulation domain in subdomains to fully utilize CUDA thread blocks. The purple area represents one subdomain, which have its pressure values calculated by a 32×32 thread block. The pink area represents the memory containing the pressure values necessary for this calculation, which is $2N$ pixels wider and higher than the subdomain, where N is the spatial Laplacian precision. This pink area is copied only once to the SM shared memory, minimizing RAM access.

where f is a n -dimensional twice-differentiable real-valued function. Since Equation (12) applies ∇^2 to the discretized function $u(x, t)$, the partial derivatives must be approximated by finite differences. Our approach applies a central difference approximation, given by

$$\frac{\partial^2 f}{\partial x^2}(x) = f''(x) \approx \frac{\sum_{i=-n}^n c_i f(x + i \cdot h)}{h^2} \quad (14)$$

where n is the approximation order, h is the discretization step and c are the coefficients given by Taylor's theorem. This paper utilizes a central difference fourth-order approximation, as suggested in [37], resulting in each finite difference using 9 points for the derivative approximation. As shown in Equation (13), this finite difference is applied in each dimension of the function. The proposed method uses 2-D media, therefore each calculation of the Laplacian operator in the update equation (12) uses 18 pressure values, resulting in 17 memory accesses because the central term in each partial derivative is the same point. The stencil for this approximation is shown in Figure 4.

Since this approximation uses 17 pressure values, 17 different memory positions need to be accessed. Considering that our 32×32 thread blocks have 1024 threads, each block iteration accesses RAM more than 17,000 times. RAM access is a computational bottleneck, so optimization is desired. This is achieved in [37] using CUDA shared

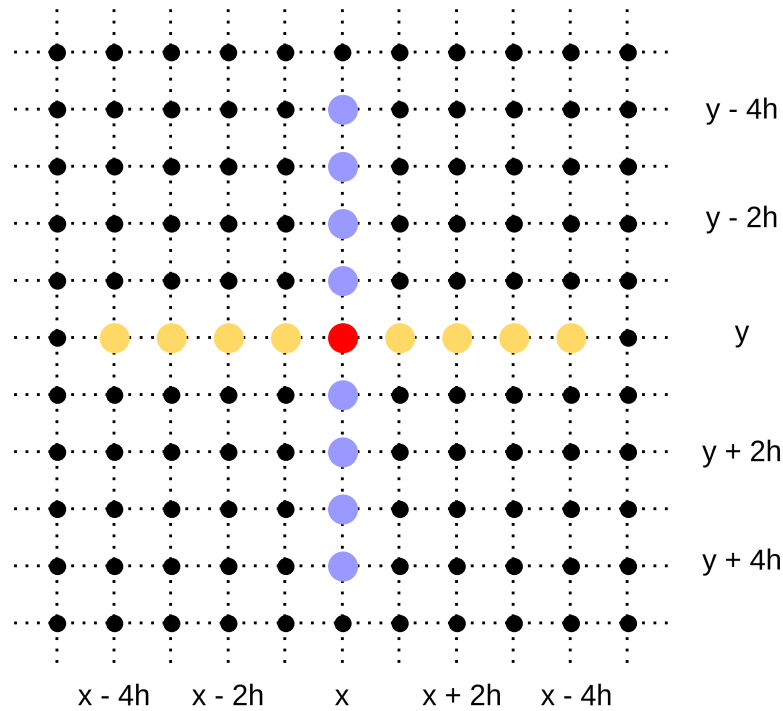


Figure 4: Fourth-order 2-D Laplacian approximation cross stencil. To approximate the Laplacian in the point (x, y) represented as the red circle, its neighbours in each dimension are used. The purple positions are used to approximate $\frac{\partial^2 u}{\partial y^2}$, and the yellow positions are used to approximate $\frac{\partial^2 u}{\partial x^2}$.

memory.

In CUDA, each thread block is executed in a Streaming Multiprocessor (SM), which has a local memory block similar to cache memory in CPUs. Since our disposition of thread blocks is composed of spatially contiguous points, and the Laplacian operator utilizes neighboring points, most RAM accesses from the same thread block will be repeated many times. To optimize memory access, our algorithm first copies the content of all RAM positions needed for the thread block Laplacian calculations to the SM shared memory, vastly reducing the number of RAM accesses and making them in sequential order, which is faster. Then, the threads use the data stored in this shared memory, improving performance.

The amount of data necessary depends on the precision of the Laplacian operator, as shown in Figure 3. The exact size of the shared memory available per SM depends on the GPU, but its small size is a limiting factor in the precision of the Laplacian approximation. Algorithm 1 outlines the process of copying data into shared memory. The memory copy is executed only by the kernels in the first line of the thread block. Each thread copies the data in a 32-register stride, so the group copies 32 contiguous memory positions in parallel, optimizing memory access.

Algorithm 1: Shared memory copy

```

 $x, z \leftarrow$  thread coordinates inside thread block;
 $x_b, z_b \leftarrow$  thread block location coordinates in global memory;
 $prec\_deriv \leftarrow$  Laplacian number of points in approximation;
 $shared\_width \leftarrow (32 + 2 * prec\_deriv)$ ;
 $shared\_size \leftarrow shared\_width^2$ ;
if  $z = 0$  // if this kernel instance is being executed on a pixel of
    the first line
then
    for (  $idx = x$ ;  $idx < shared\_size$ ;  $idx = idx + 32$  )
        // point coordinates in shared memory
         $x_s \leftarrow \lfloor idx / shared\_width \rfloor$ ;
         $z_s \leftarrow idx \bmod shared\_width$ ;
        // point coordinates in global memory
         $x_g \leftarrow x_b - prec\_deriv + x_s$ ;
         $z_g \leftarrow z_b - prec\_deriv + z_s$ ;
        // memory copy from global to shared
         $shared[z_s][x_s] \leftarrow global[z_g][x_g]$ ;
    end
end

```

3.2. Low memory gradient computation

The adjoint state method for FWI obtains the misfit metric gradient w.r.t. the sound speed field using the direct and adjoint fields, as shown in Equation (15):

$$\gamma(\theta) = \int_I \tilde{u}(T-t) \nabla^2 u(t) dt, \quad (15)$$

where θ is the sound speed, $\gamma(\theta)$ is the gradient, u is the direct field, I is the simulated time interval, and \tilde{u} is the adjoint field defined in Eq. (8). Since \tilde{u} is time-reversed, the equation resembles a correlation between the adjoint field and the Laplacian of the direct field, and has been interpreted this way by some authors [34].

The reversal of the adjoint field arises from the necessary condition that its value at $t = T$ be zero so that the wave equation simulator is self-adjoint. Since memory limitations force virtually all simulator implementations to be explicit, i.e., time-marching, and the wave equation is time-symmetrical, it is easier to simulate the adjoint field backward by back-propagating the adjoint source signals. By adopting this convention, the time notation becomes

$$\gamma(\theta) = \int_I \tilde{u}(t) \nabla^2 u(t) dt. \quad (16)$$

This poses a problem: both fields are needed at the same time to calculate the gradient, but they are not fully stored in the proposed low-memory method. One apparent

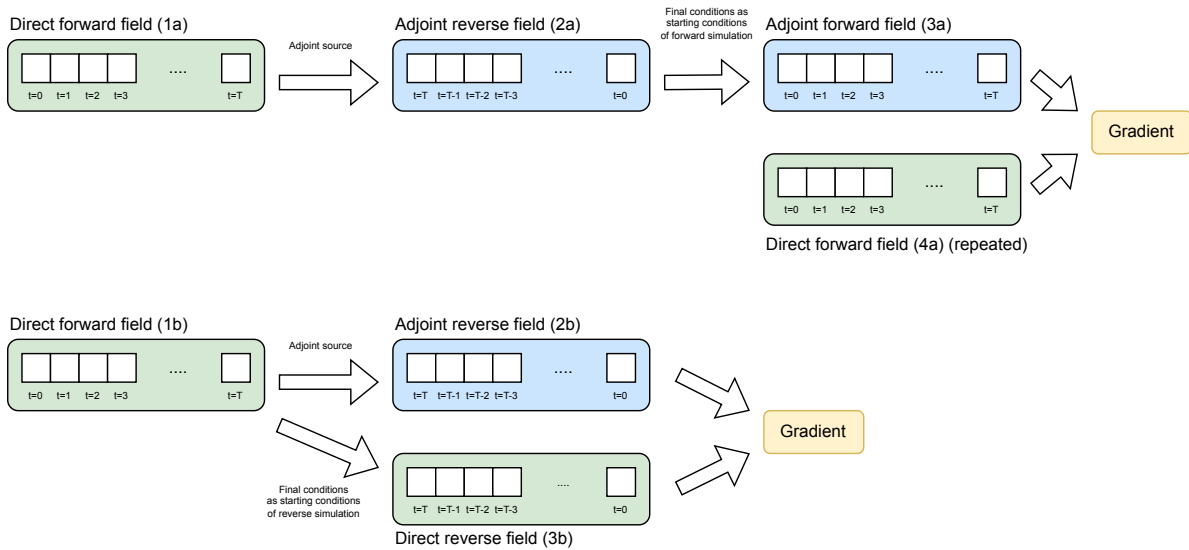


Figure 5: Simulating fields backward to parallelize gradient calculation. Both schemes first calculate the direct field (1a and 1b) to obtain the metric value and adjoint source signals. At the top, after the first simulation (1a), the adjoint field (2a) is simulated to obtain the starting conditions for the reversed adjoint field (3a), which is run in parallel with the direct field again (4a). At the bottom, the final conditions of the first simulation (1b) are used as the starting conditions for the second simulation (2b), which runs in parallel with the third (3b). On both, the parallelized fields are used to obtain the gradient. [28].

solution is to simulate them simultaneously, but we necessarily simulate \tilde{u} backward. To achieve this parallelism, one of the simulations must be reversed, the adjoint [27] or the direct [28].

To simulate a field backward, one needs only the final conditions as the starting conditions of the new simulation and reverse the source signals. Thus, to achieve this time reversal, one of the fields must be simulated twice. Since the adjoint source needs the direct field to be calculated, this field already needs to be simulated twice for the low-memory method, so it is chosen to be reversed. It is shown in [28] that reversing the adjoint field would need one additional simulation, increasing computational cost. Figure 5 shows both schemes.

The final algorithm is shown in Figure 6. The simulations and gradient computation are performed on the GPU, while the minimization algorithm runs on the CPU. The adjoint source and misfit can be calculated at either one.

3.3. Wasserstein distance as misfit metric for FWI

To tackle the cycle-skipping phenomena, the W_2^2 Wasserstein metric is used. This metric is defined as

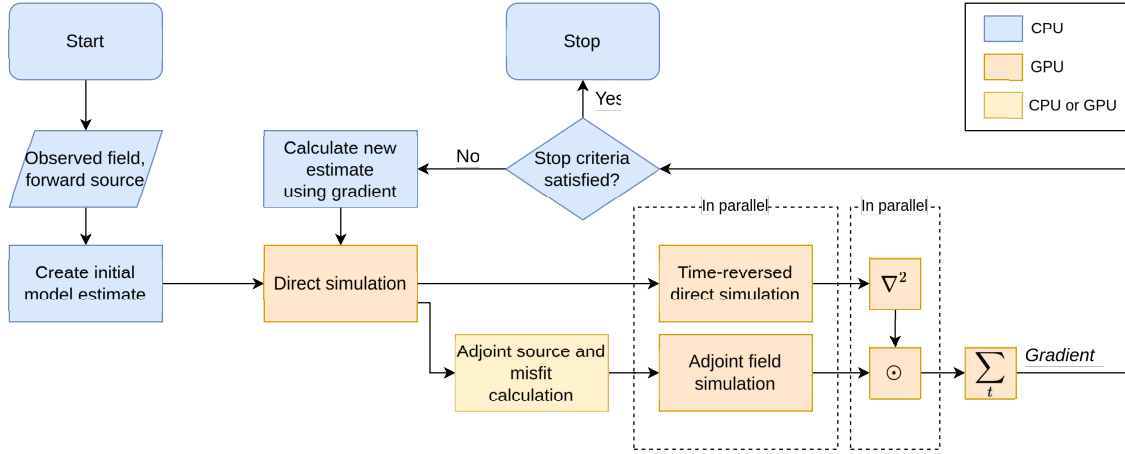


Figure 6: FWI algorithm implemented using GPU parallelism.

$$W_2^2(f, g) = \inf_{T \in \mathcal{M}} \int_X |x - T(x)|^2 f(x) dx, \quad (17)$$

where “inf” is the infimum and \mathcal{M} is the set of all transportation plans that transform f into g [24]. This metric has the advantage of being highly insensitive to noise and convex in relation to signal shift, dilation, and partial amplitude change [29]. In another possible interpretation, $W_2^2(f, g)$ can be seen as a measure of misfit between the PDFs f and g .

However, FWI deals with acoustic signals and, thus, two key characteristics of the signals must be adapted to resemble PDFs so that the metric may be applied: positivity and mass balance. Namely, both signals must have their integrals equal to 1 and be strictly positive. This paper employs the approach proposed in [15], consisting of linear transformation and scaling:

$$c = 1.1 \cdot |g_{min}|, \quad (18)$$

$$P(f) \equiv \frac{f + c}{\langle f + c \rangle} \quad (19)$$

where g is the observed signal, c is an offset constant, and P is the transformation to be applied in the observed and simulated signals to obtain the modified f and g , adequate for calculating the Wasserstein metric using (17). Although this approach yields worse cycle-skipping than separating the positive and negative parts of the signals in the case of simple pulse shifting, its performance in the more complex waveforms in FWI is better [15, 21]. This effect is shown in Figure 7, using the same pulses as in Figure 2.

The Wasserstein distance definition (17) is a minimization problem, and must be numerically solved to obtain the metric value if the PDFs f and g have more than one dimension [35]. However, if f and g are unidimensional variables, there is an analytical

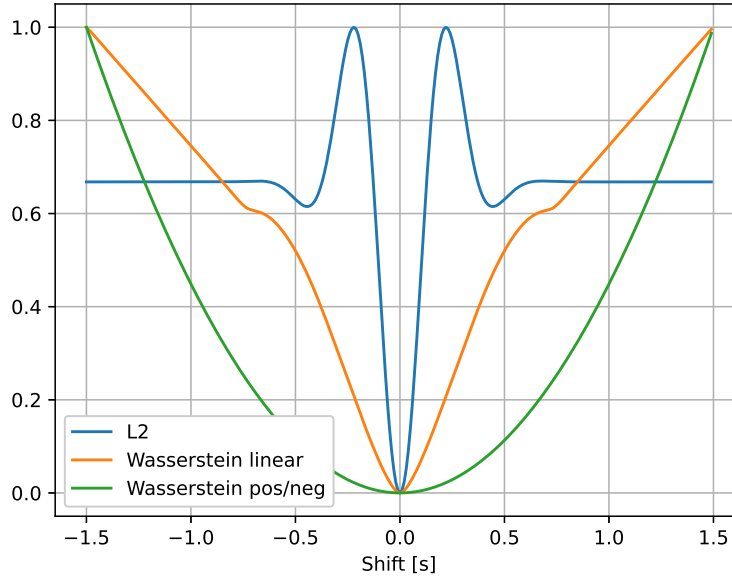


Figure 7: Normalized misfit metrics for shifted Gaussian pulses.

solution given by

$$W_2^2(f, g) = \int_0^1 |x - G^{-1}(F(x))|^2 f(x) dx, \quad (20)$$

$$F(x) = \int_{-\infty}^x f(x) dx, \quad G(x) = \int_{-\infty}^x g(x) dx, \quad (21)$$

where F and G are the cumulative probability functions (CDFs) of f and g respectively. To use the adjoint state method to obtain the derivative w.r.t. the sound speed parameters, it is necessary to obtain the derivative of (21) w.r.t. f and use it as the source term of the adjoint simulation. This source term is given by

$$\frac{\partial W_2^2}{\partial f}(t) = -2 \int_t^T [x - G^{-1}(F(x))] dx. \quad (22)$$

The complete derivation is available in Appendix A.

3.4. Simulated setup

To evaluate the proposed approach, an inspection setup was simulated with six different speed models. The setup is schematized in Figure 8: two 64-element array transducers are immersed in water ($c_w = 1450$ m/s) facing each other with a 110 mm distance. The pitch (distance between elements of the same array) is 1.59 mm. All 128 elements operate as individual receivers. Elements 1, 16, 32, 48, and 64 from both arrays also operate as emitters. Thus, the dimensions of the data matrix are $N_e \times N_r \times N_s$, where $N_e = 10$ is the number of emitting elements, $N_r = 128$ is the number of receiving

elements, and N_s is the number of time samples recorded during each emission. The emitted pulse is a Ricker wavelet given by

$$s(t; f_0, b) = \exp \left[-\frac{(b\pi f_0 t)^2}{\ln \sqrt{2}} \right] \sin(2\pi f_0 t), \quad (23)$$

where $b = 90\%$ is the width of the half-power bandwidth, and $f_0 = 1$ MHz is the center frequency. This wavelet and its frequency spectrum are shown in Figure 9.

The simulated domain is larger than the limits of the arrays, with $150 \text{ mm} \times 150 \text{ mm}$, discretized in $300 \text{ }\mu\text{m}$ in both x and y axes, making 2.5×10^5 pixels. The 20 outermost layers of the simulated domain were used to implement PML, as described in [20]. The time dimension was discretized in 25 ns units. The simulations were run for $200 \text{ }\mu\text{s}$.

Six different speed models were simulated, shown in Figure 10:

- Specimen I - Camembert model: a 3600 m/s circle in a 3000 m/s medium
- Specimen II - Acrylic square with 2 side-drilled holes
- Specimen III - Steel square
- Specimen IV - Steel square with circular hole
- Specimen V - Steel square with 2 side-drilled holes
- Specimen VI - Acrylic star

3.5. Model reconstruction

To solve the FWI optimization problem, the L-BFGS-B algorithm [38] was used, limited to 200 iterations, with the gradients computed via adjoint state method as described in Section 3.2. All the simulations performed within the optimization algorithm to compute the gradients and evaluate partial solutions were run with the same configurations as described in Section 3.4. Every initial model is a uniform field with a sound speed $c = 1450 \text{ m/s}$, except for Specimen I, which used $c = 3000 \text{ m/s}$.

4. Results

The results of the FWI algorithm with the proposed Wasserstein source term are shown in Figures 11 and 12, compared with the regression with L2 source term and a TFM reconstruction. The FWI regressions did not have any prior information about the specimen, so the TFM images also did not have the information about the surface and material to compensate for the travel time to points inside the specimen.

The evolution of the misfit across the iterations of the L-BFGS-B algorithm is shown in Figure 13. The W_2^2 misfit between the soundwaves - the metric that is effectively being minimized - is shown in 13a. The Mean Square Error (MSE) between the ground truth and the estimated models are shown in 13b. It is important to note that this metric is not accessible to the algorithm during the minimization. The minimization for models A and F ended before the 200 iteration limit due to convergence.

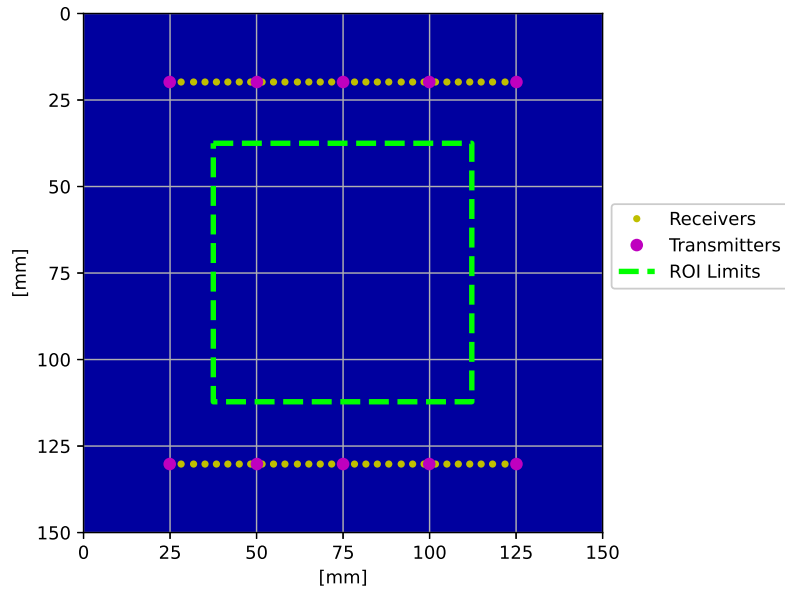


Figure 8: Simulated setup.

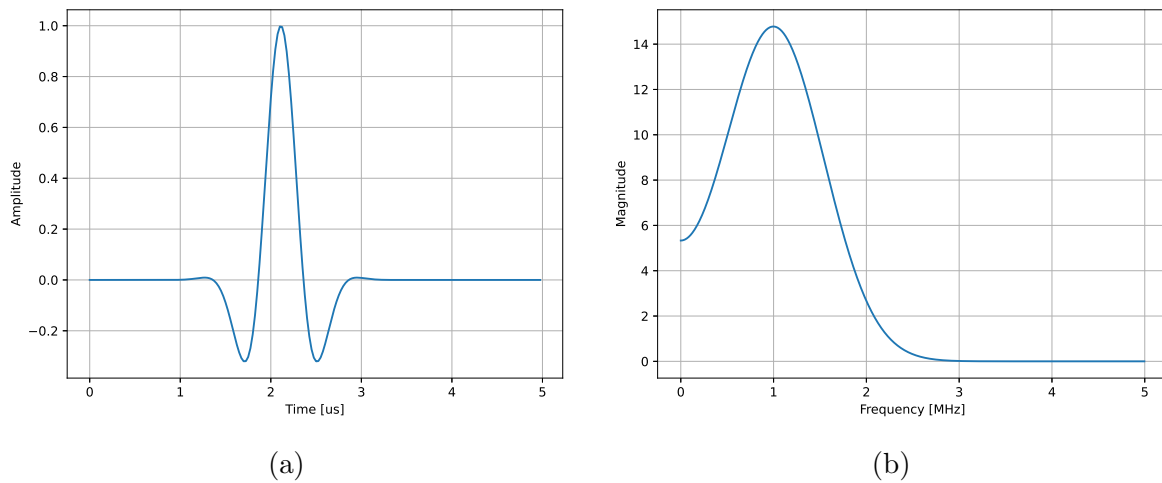


Figure 9: The Ricker wavelet used as excitation pulse for simulated inspections. (a) Time-domain plot. (b) Magnitude spectrum.

The final values for the misfits, as well as the computation time for each minimization, are shown in Table 1. These times were obtained using an NVIDIA Titan XP GPU.

To exemplify the evolution of the estimate during the minimization, some intermediary results from Specimen II are shown in Figure 14.

4.1. Discussion

Comparing the sound speed map obtained from the Wasserstein-FWI framework with the true models, it is clear that this method struggles to reconstruct sharp speed

differences. Specimens I, II, and VI have lower speed differences than Specimens III, IV, and V, and had much better results. However, this is a known limitation of FWI. The only specimen where the L2-FWI framework obtained a good result was Specimen I, which has the lowest speed difference in the set. Wasserstein-FWI converged to much better results on all other specimens.

In the high-speed difference specimens, III and V obtained better external surface estimation than IV. However, while Specimen IV was unable to reconstruct the lateral boundaries of the specimen, this is a common problem in ultrasound tests where the wavefronts are not perpendicularly incident to the surface. This could be remedied by using ultrasonic elements on all sides of the specimen, rather than only on two sides; however, this is not a common ultrasound array configuration.

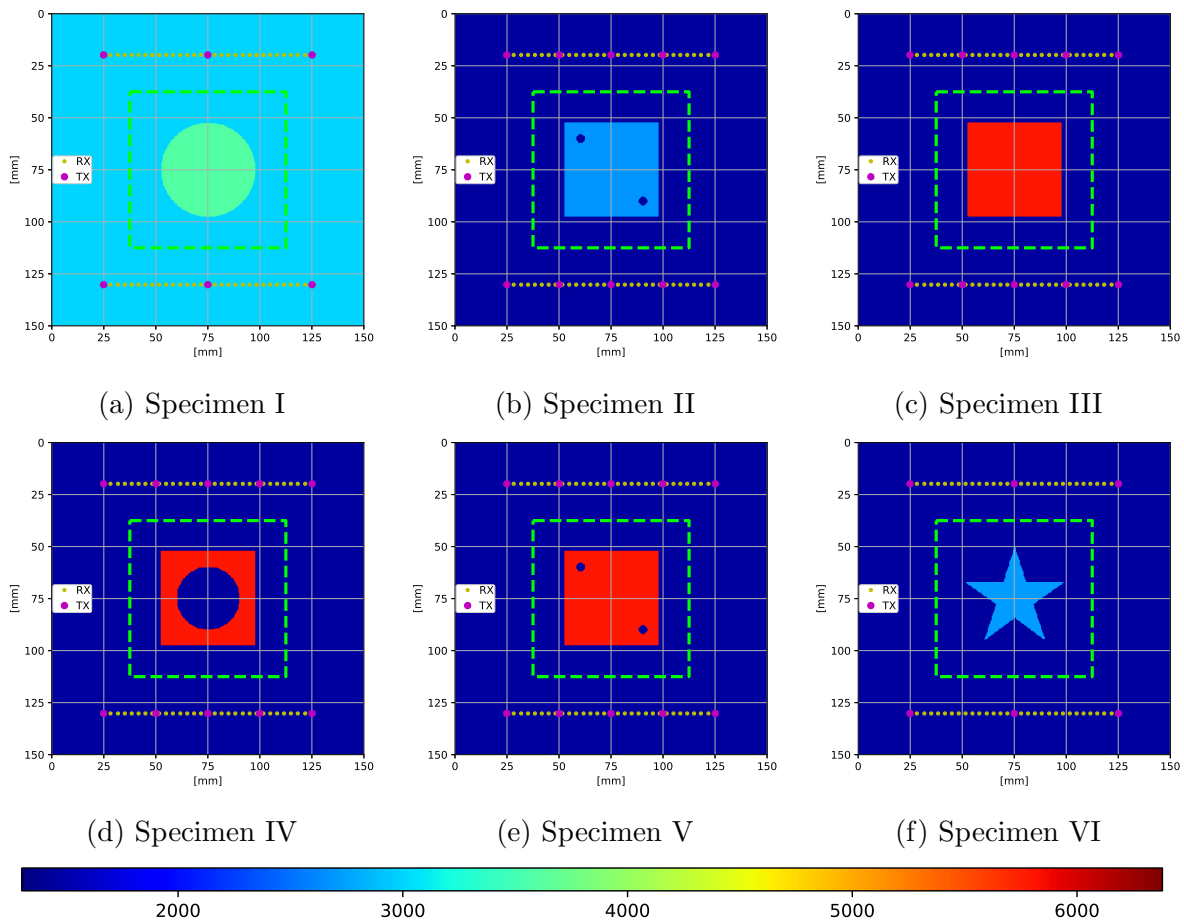


Figure 10: Speed fields for the test specimens. Specimen I is the Camembert model, Specimen II is an acrylic square with two side drill holes, Specimen III is a steel square, Specimen IV is a steel square with a circular hole, Specimen V is a steel square with two side drill holes, and Specimen VI is an acrylic star. The specimens were simulated with 10 sources and 64 receivers, evenly distributed above and below the specimens. The dashed green square is the sensitivity kernel, and the colors represent the medium sound speed.

5. Conclusions

To improve the quality of ultrasound images obtained in NDT, this paper presented a method to apply Full Waveform Inversion – traditionally used in seismic prospecting – to signals obtained from ultrasonic arrays. NDT specimens usually have sharper and higher sound speed difference interfaces [21], which amplify the cycle-skipping problem [13]. Not only that, but typical ultrasound signals lack low-frequency components. To mitigate this problem, the Wasserstein metric is applied. As theoretically expected, the proposed method is able to generate fairly accurate sound speed maps, with the Wasserstein metric obtaining good results where the traditional L_2^2 metric could not converge.

The proposed Wasserstein source term performed better than the traditional L_2^2 metric. The final models obtained using the W_2^2 have better model MSE and better waveform L_2^2 misfit than the models obtained with the L_2^2 cost function. The computational cost to evaluate the W_2^2 cost function is higher than the L_2^2 , but still much lower than the computation cost of the acoustic simulation. Therefore, the total time increase is almost negligible, in the 2% range, as shown in Table 1.

Further improvements can be expected with a more advanced wave simulator, for

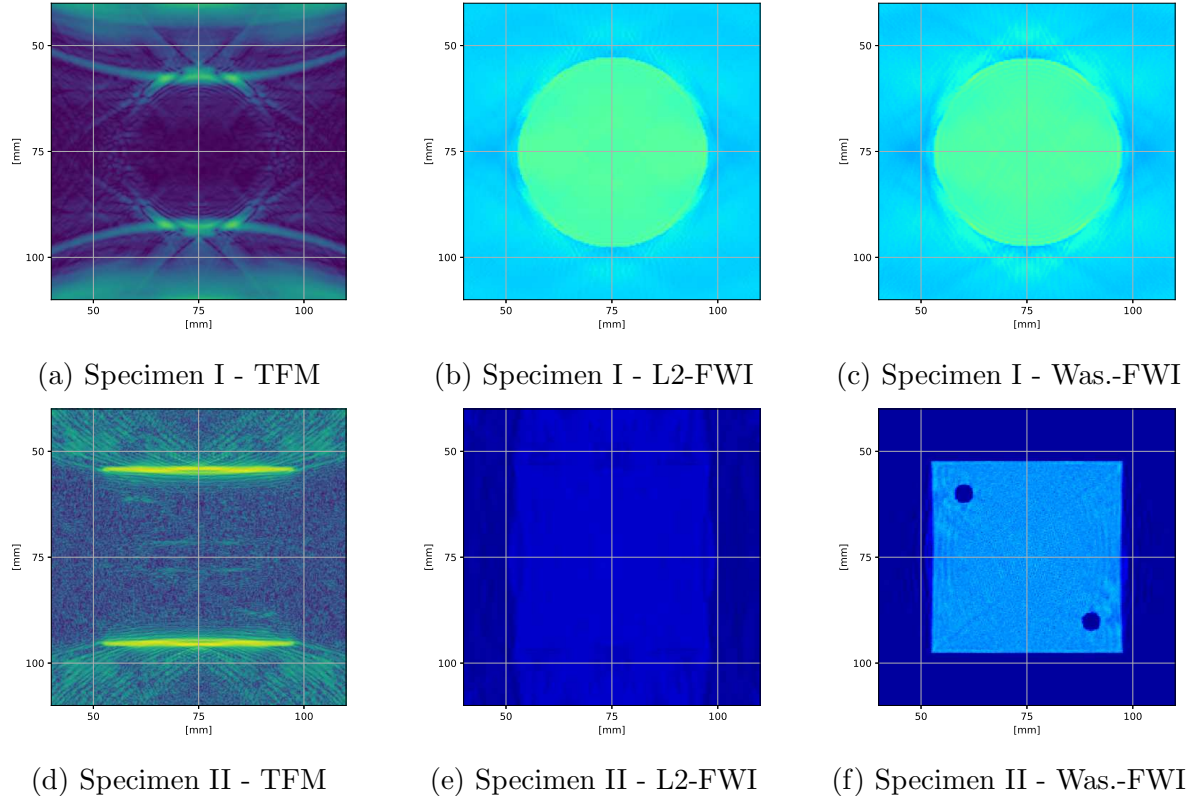


Figure 11: Image reconstructions from Specimens I and II using TFM, L2-FWI and Wasserstein-FWI. Only the area inside the sensitivity kernel is shown. The sound speed scale used in the FWI reconstructions is the same as used in Figure 10.

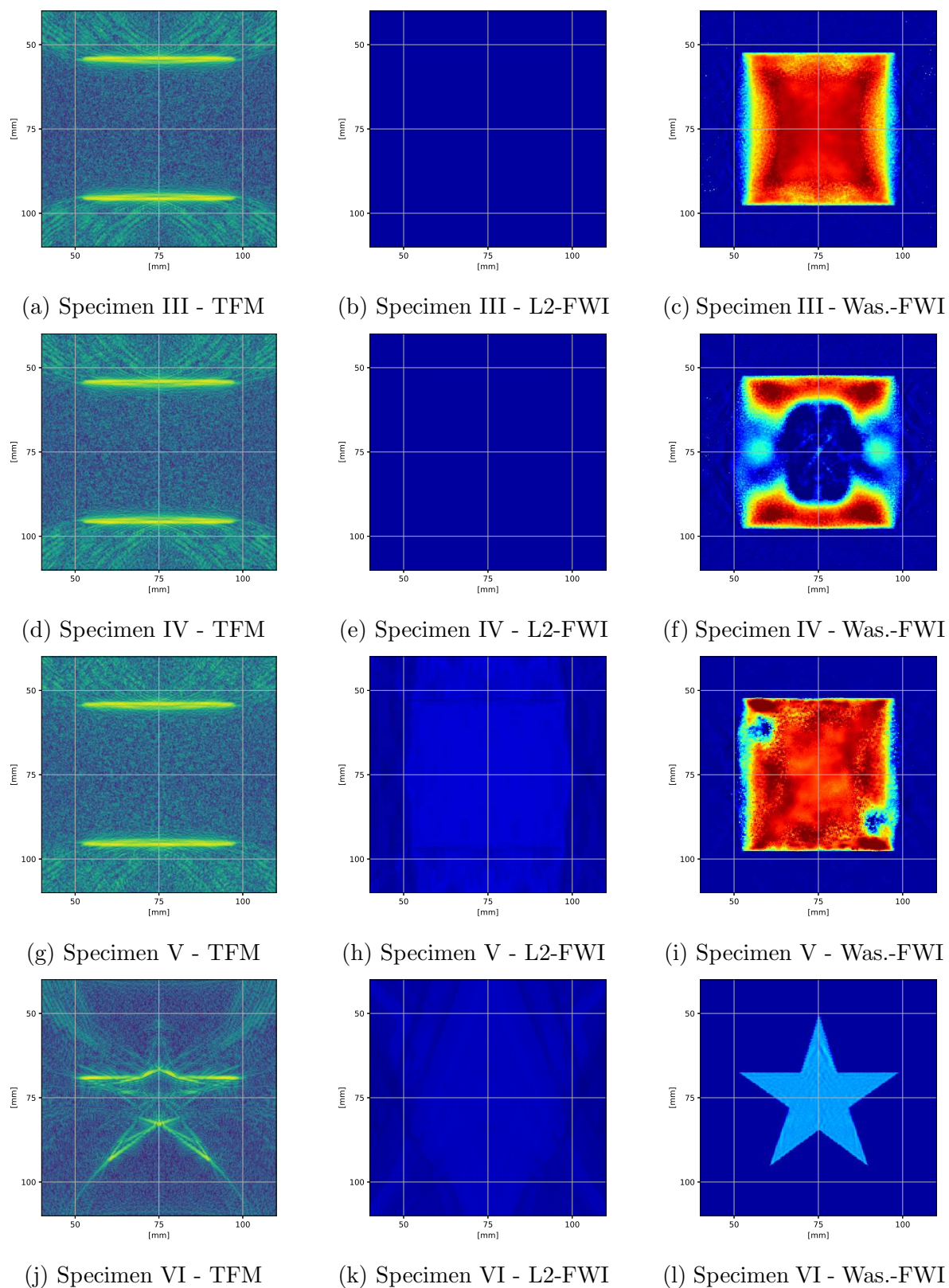


Figure 12: Image reconstructions from Specimens III through VI using TFM, L2-FWI and Wasserstein-FWI. Only the area inside the sensitivity kernel is shown. The sound speed scale used in the FWI reconstructions is the same as used in Figure 10.

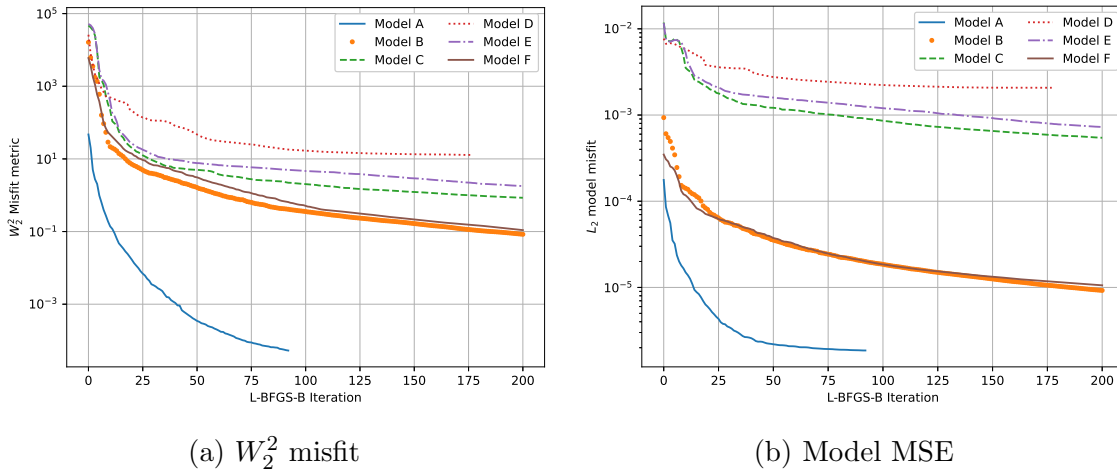


Figure 13: Evolution of model estimate during L-BFGS-B minimization using the W_2^2 cost function. In (a) is the W_2^2 misfit between acquired and simulated (from current model guess) waveforms, and (b) shows the MSE between ground truth and estimated models.

example, by using a viscoelastic model instead of the acoustic wave. Different Laplacian operator approximations, such as the radiation stencil, have also shown improvements in simulations [39, 40]. The directivity of the transducer arrays can also be incorporated

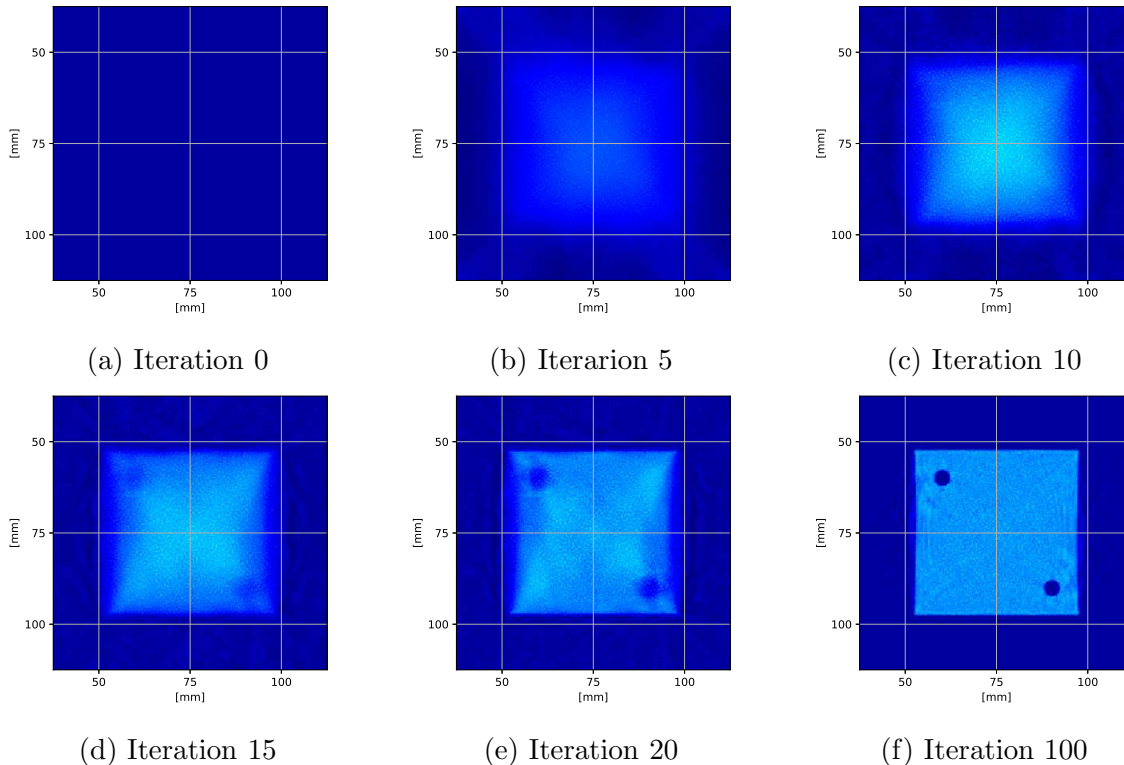


Figure 14: Sound speed estimates during the L-BFGS-B minimization in Specimen II.

C_{L_2} misfit						
Specimen	I	II	III	IV	V	VI
L2-FWI	5.05e-02	2.38e+03	2.99e+03	2.97e+03	2.65e+03	1.90e+03
W2-FWI	3.70e-02	4.62e+01	3.45e+02	7.46e+02	2.87e+02	1.61e+02

C_{W_2} misfit						
Specimen	I	II	III	IV	V	VI
L2-FWI	2.80e-05	1.33e+01	1.08e+01	6.07e+00	3.49e+01	1.70e+00
W2-FWI	3.50e-07	1.50e-03	1.67e-02	2.41e-01	3.07e-02	3.06e-03

Model MSE						
Specimen	I	II	III	IV	V	VI
L2-FWI	1.27e-06	6.82e-04	1.18e-02	7.67e-03	1.05e-02	3.20e-04
W2-FWI	1.86e-06	9.23e-06	5.45e-04	2.07e-03	7.27e-04	1.06e-05

Gradient computation time [s]						
Specimen	I	II	III	IV	V	VI
L2-FWI	62.4	63.5	63.8	64.3	62.2	61.2
W2-FWI	63.7	64.3	64.7	65.3	63.8	63.9

Table 1: Numerical results from the minimizations using L_2^2 and W_2^2 cost functions.

into the simulator [14], as well as 3D media. Physics-informed neural networks are also being studied for these simulations [41].

Other positivity criteria remain to be tested in this framework, such as the Graph-Space Optimal Transport [16], as well as some form of regularization. Total variation regularization is a promising alternative [42], since the specimens in NDT usually have continuous areas with the same sound speed. Another promising approach is the travel-time FWI [43].

Source code availability

All source codes needed for the reproduction of the results presented in this paper are available at <https://github.com/lassip-utfpr/Otfwi>.

Acknowledgements

The authors thank UTFPR, CAPES, Fundação Araucária, FINEP, CNPq (grant number 305075/2025-0), and Petrobras (SIGITEC 2022/00436-2) for the scholarships and funding. The authors declare no other conflict of interest.

Appendix A. Proof of the source term for the continuous analytical solution of the 1-D Wasserstein metric

The solution for the 1-D Wasserstein distance is given [35] by

$$W_2^2(t) = \int_0^t [F^{-1}(t) - G^{-1}(t)]^2 dt. \quad (\text{A.1})$$

To obtain the source term of the adjoint problem, we derive this distance w.r.t. $f(t)$:

$$\frac{\partial W_2^2}{\partial f}(t) = \frac{\partial}{\partial f} \int_0^t [F^{-1}(t) - G^{-1}(t)]^2 dt \quad (\text{A.2})$$

$$= \int_0^t 2 \left[(F^{-1}(t) - G^{-1}(t)) \left(\frac{\partial F^{-1}(t)}{\partial f} - \frac{\partial G^{-1}(t)}{\partial f} \right) \right] dt. \quad (\text{A.3})$$

The partial derivatives inside the parenthesis are

$$\frac{\partial G^{-1}(t)}{\partial f} = 0, \quad (\text{A.4})$$

$$\frac{\partial F^{-1}(t)}{\partial f} = \frac{\partial F^{-1}(t)}{\partial t} \frac{\partial t}{\partial f}. \quad (\text{A.5})$$

By the inverse function theorem, we have

$$(a^{-1})'(b) = \frac{1}{a'(a^{-1}(b))}, \quad (\text{A.6})$$

therefore, applying this theorem to (A.5),

$$\frac{\partial F^{-1}(t)}{\partial f} = \frac{\partial F^{-1}(t)}{\partial t} \frac{\partial t}{\partial f} = \frac{1}{f(F^{-1}(t))} \frac{\partial t}{\partial f}. \quad (\text{A.7})$$

Inserting (A.4) and (A.7) back into (A.3), we have

$$\frac{\partial W_2^2}{\partial f}(t) = 2 \int_0^t (F^{-1}(t) - G^{-1}(t)) \frac{1}{f(F^{-1}(t))} \frac{\partial t}{\partial f}(t) dt \quad (\text{A.8})$$

Changing variables:

$$t = F(x), \quad x = F^{-1}(t), \quad dt = f(x) dx \quad (\text{A.9})$$

$$\frac{\partial W_2^2}{\partial f}(t) = 2 \int_0^t [F^{-1}(F(x)) - G^{-1}(F(x))] \cdot \left[\frac{1}{f(F^{-1}(F(x)))} \frac{\partial t}{\partial f}(F(x)) \right] f(x) dx \quad (\text{A.10})$$

$$\frac{\partial W_2^2}{\partial f}(t) = 2 \int_0^t [x - G^{-1}(F(x))] \cdot \left[\frac{1}{f(x)} \frac{1}{f'(F(x))} \right] f(x) dx \quad (\text{A.11})$$

$$\frac{\partial W_2^2}{\partial f}(t) = 2 \int_0^t [x - G^{-1}(F(x))] \left[\frac{f(x)}{f(x)} \frac{1}{f'(F(x))} \right] dx \quad (\text{A.12})$$

Now we change variables again to apply the inverse function theorem (A.6) to the term $\frac{1}{f'(F(x))}$:

$$k(x) = f^{-1}(x), \quad f(x) = k^{-1}(x) \quad (\text{A.13})$$

$$f'(F(x)) = (k^{-1})'(F(x)) \quad (\text{A.14})$$

$$= \frac{1}{k'(k^{-1}(F(x)))} = \frac{1}{(f^{-1})'(f(F(x)))} \quad (\text{A.15})$$

$$= \frac{1}{\frac{\partial}{\partial t} f^{-1}(f(t))} = \frac{1}{\frac{\partial t}{\partial t}} = 1 \quad (\text{A.16})$$

Inserting (A.16) into (A.12):

$$\frac{\partial W_2^2}{\partial f}(t) = 2 \int_0^t [x - G^{-1}(F(x))] dx. \quad (\text{A.17})$$

The boundary conditions for the self-adjointness of the acoustic wave operator specify that this source term must end in zero. Therefore, one must add an offset C so $\frac{\partial W_2^2}{\partial f}(T) = 0$:

$$\frac{\partial W_2^2}{\partial f}(T) = 2 \int_0^T [x - G^{-1}(F(x))] dx + C = 0 \quad (\text{A.18})$$

$$C = -2 \int_0^T [x - G^{-1}(F(x))] dx \quad (\text{A.19})$$

$$\frac{\partial W_2^2}{\partial f}(t) = 2 \int_0^t [x - G^{-1}(F(x))] dx - 2 \int_0^T [x - G^{-1}(F(x))] dx \quad (\text{A.20})$$

$$\frac{\partial W_2^2}{\partial f}(t) = -2 \left\{ \int_0^T [x - G^{-1}(F(x))] dx - \int_0^t [x - G^{-1}(F(x))] dx \right\} \quad (\text{A.21})$$

Since the terms inside the integrals are equal, we can join them by changing only the integration limits, to finally arrive at the source term for the continuous 1-D Wasserstein adjoint problem:

$$\frac{\partial W_2^2}{\partial f}(t) = -2 \int_t^T [x - G^{-1}(F(x))] dx. \quad (\text{A.22})$$

References

- [1] Lester W. Schmerr. *Fundamentals of Ultrasonic Phased Arrays*, volume 215. Springer International Publishing, 2015.
- [2] Caroline Holmes, Bruce W. Drinkwater, and Paul D. Wilcox. Post-processing of the full matrix of ultrasonic transmit-receive array data for non-destructive evaluation. *NDT and E International*, 38:701–711, 12 2005.

- [3] Albert Tarantola. Inversion of seismic reflection data in the acoustic approximation. *GEOPHYSICS*, 49:1259–1266, 8 1984.
- [4] J. Virieux and S. Operto. An overview of full-waveform inversion in exploration geophysics. *GEOPHYSICS*, 74:WCC1–WCC26, 11 2009.
- [5] Rongxin Huang, Zhigang Zhang, Zedong Wu, Zhiyuan Wei, Jiawei Mei, and Ping Wang. Full-waveform inversion for full-wavefield imaging: Decades in the making. *The Leading Edge*, 40:324–334, 5 2021.
- [6] Jeroen Tromp. Seismic wavefield imaging of earth’s interior across scales. *Nature Reviews Earth and Environment*, 1:40–53, 1 2020.
- [7] Rehman Ali, Trevor M. Mitcham, Thurston Brevett, Òscar Calderón Agudo, Cristina Durán Martínez, Cuiping Li, Marvin M. Doyley, and Nebojsa Duric. 2-D slice-wise waveform inversion of sound speed and acoustic attenuation for ring array ultrasound tomography based on a block LU solver. *IEEE Transactions on Medical Imaging*, pages 1–1, 2024.
- [8] P. Lailly. The seismic inverse problem as a sequence of before stack migrations. In *Conference on Inverse Scattering, Theory and application*, pages 206–220, 1983.
- [9] Odile Gauthier, Jean Virieux, and Albert Tarantola. Two-dimensional nonlinear inversion of seismic waveforms: Numerical results. *GEOPHYSICS*, 51:1387–1403, 7 1986.
- [10] Carey Bunks, Fatimetou M. Saleck, S. Zaleski, and G. Chavent. Multiscale seismic waveform inversion. *GEOPHYSICS*, 60:1457–1473, 9 1995.
- [11] R G Pratt, Z.-M Song, P Williamson, and M Warner. Two-dimensional velocity models from wide-angle seismic data by wavefield inversion. *Geophys. J. Int*, 124:323–340, 1996.
- [12] Gerhard Pratt, Changsoo Shin, and Hicks. Gauss-newton and full newton methods in frequency-space seismic waveform inversion. *Geophysical Journal International*, 133:341–362, 5 1998.
- [13] Zedong Wu, Zhiyuan Wei, Zhigang Zhang, Jiawei Mei, Rongxin Huang, and Ping Wang. Elastic FWI for large impedance contrasts. In *Proceedings of the Second International Meeting for Applied Geoscience and Energy*, pages 3686–3690. Society of Exploration Geophysicists and American Association of Petroleum Geologists, 8 2022.
- [14] Xiaoqing Wu, Yubing Li, Chang Su, Panpan Li, and Weijun Lin. Optimal transport assisted full waveform inversion for multiparameter imaging of soft tissues in ultrasound computed tomography. *Ultrasonics*, page 107505, 11 2024.
- [15] Yunan Yang, Björn Engquist, Junzhe Sun, and Brittany F. Hamfeldt. Application of optimal transport and the quadratic Wasserstein metric to full-waveform inversion. *Geophysics*, 83, 2018.
- [16] Ludovic Métivier, Aude Allain, Romain Brossier, Quentin Méridot, Edouard Oudet, and Jean Virieux. Optimal transport for mitigating cycle skipping in full-waveform inversion: A graph-space transform approach. *GEOPHYSICS*, 83:R515–R540, 9 2018.
- [17] Xingpeng Dong, Dinghui Yang, and Hejun Zhu. Optimal transport map with prescribed direction indicator for seismic full-waveform inversion. *Journal of Geophysical Research: Solid Earth*, 129, 7 2024.
- [18] Robert Seidl and Ernst Rank. Iterative time reversal based flaw identification. *Computers and Mathematics with Applications*, 72:879–892, 8 2016.
- [19] Robert Seidl and Ernst Rank. Full waveform inversion for ultrasonic flaw identification. In *AIP Conference Proceedings*, volume 1806. American Institute of Physics Inc., 2 2017.
- [20] Felipe Derewlany Gutierrez, Daniel Rossato, Gustavo P. Pires, Thiago Alberto Rigo Passarin, Giovanni A. Guarneri, and Daniel Rodrigues Pipa. Using perfectly matched layer in a GPU simulation of ultrasound NDT. *Research and Review Journal of Nondestructive Testing*, 1, 8 2023.
- [21] Daniel Rossato, Felipe Derewlany Gutierrez, Giovanni A. Guarneri, Thiago Alberto Rigo Passarin, Gustavo P. Pires, and Daniel Rodrigues Pipa. Full waveform inversion for NDT using ultrasonic linear arrays. *Research and Review Journal of Nondestructive Testing*, 1, 8 2023.
- [22] Arnaud Pladys, Romain Brossier, Yubing Li, and Ludovic Métivier. On cycle-skipping and

- misfit function modification for full-wave inversion: Comparison of five recent approaches. *GEOPHYSICS*, 86:R563–R587, 7 2021.
- [23] Ebru Bozdağ, Jeannot Trampert, and Jeroen Tromp. Misfit functions for full waveform inversion based on instantaneous phase and envelope measurements. *Geophysical Journal International*, 185:845–870, 5 2011.
- [24] Björn Engquist and Brittany D. Froese. Application of the Wasserstein metric to seismic signals. *Communications in Mathematical Sciences*, 12:979–988, 11 2014.
- [25] Nuomin Zhang, Yang Xiao, Yu Yuan, Xudong Yang, and Yi Shen. Full-waveform inversion with low-frequency extrapolation based on sparse deconvolution for ultrasound computed tomography. *Ultrasound in Medicine and Biology*, 5 2025.
- [26] Qing-Huo Liu and Jianping Tao. The perfectly matched layer for acoustic waves in absorptive media. *The Journal of the Acoustical Society of America*, 102(4):2072–2082, 1997.
- [27] Reynaldo F. Noriega, Ana B. Ramirez, Sergio A. Abreo, and Gonzalo R. Arce. Implementation strategies of the seismic full waveform inversion. *ICASSP, IEEE International Conference on Acoustics, Speech and Signal Processing - Proceedings*, pages 1567–1571, 6 2017.
- [28] Reynaldo Fabian Noriega, Sergio Alberto Abreo, and Ana B. Ramirez. Accelerated 2D FWI using the symmetry on inner product spaces. *CTyF - Ciencia, Tecnología y Futuro*, 8:89–98, 7 2018.
- [29] Bjorn Engquist, Brittany D. Froese, and Yunan Yang. Optimal transport for seismic full waveform inversion. *Geophysics*, 2 2016.
- [30] Heiner Igel. *Computational seismology: a practical introduction*. Oxford University Press, 2017.
- [31] R.-E. Plessix. A review of the adjoint-state method for computing the gradient of a functional with geophysical applications. *Geophysical Journal International*, 167:495–503, 11 2006.
- [32] Benxin Chi, Lianguo Dong, and Yuzhu Liu. Full waveform inversion method using envelope objective function without low frequency data. *Journal of Applied Geophysics*, 109:36–46, 10 2014.
- [33] Eyal Shimony and Ariel Lellouch. Joint source-structure full waveform inversion using distributed acoustic sensing. *Geophysical Journal International*, 244(2):ggaf510, 2026.
- [34] Michael Warner and Lluís Guasch. Adaptive waveform inversion: Theory. *Geophysics*, 81:R429–R445, 11 2016.
- [35] Cédric Villani. *Topics in Optimal Transportation*, volume 58. American Mathematical Society, 3 2003.
- [36] NVIDIA, Péter Vingelmann, and Frank H.P. Fitzek. Cuda, release: 10.2.89, 2020.
- [37] Jinwei Fang, Hanming Chen, Hui Zhou, Ying Rao, Pengyuan Sun, and Jianlei Zhang. Elastic full-waveform inversion based on GPU accelerated temporal fourth-order finite-difference approximation. *Computers and Geosciences*, 135, 2 2020.
- [38] Jorge Nocedal and Stephen J. Wright. *Numerical optimization*. Springer, New York, NY, 2. ed. edition, 2006.
- [39] Guiting Chen, Zhenming Peng, and Yalin Li. An efficient finite-difference stencil with high-order temporal accuracy for scalar wave modeling. *Applied Sciences (Switzerland)*, 13, 1 2023.
- [40] Han Chen, Hector Klie, and Qiqi Wang. A black-box stencil interpolation method to accelerate reservoir simulations. In *Proceedings of the SPE Reservoir Simulation Symposium 2013*. SPE, 2 2013.
- [41] Majid Rasht-Behesht, Christian Huber, Khemraj Shukla, and George Em Karniadakis. Physics-informed neural networks (PINNs) for wave propagation and full waveform inversions. *J. Geophys. Res. Solid Earth*, 127(5), May 2022.
- [42] K. Aghazade, A. Gholami, and H. S.Aghamiry. Full waveform inversion by adaptive tikhonov-total variation regularization. In *Proceedings of the 84th EAGE Annual Conference and Exhibition*, volume 2, pages 1–5. European Association of Geoscientists and Engineers, 2023.
- [43] Ping Tong. Adjoint-state travelttime tomography: Eikonal equation-based methods and application to the anza area in southern california. *Journal of Geophysical Research: Solid Earth*, 126, 5 2021.